Influenza-induced activation of recruited alveolar macrophages during the early inflammatory phase drives lung injury and lethality

Clarissa M Koch[1], Kishore Anakella[1], Jennifer Yuan-Shi Hu[1], Mark Ciesielski[1], Gaurav Gadhvi[2], Sam Chen[2], Maggie Turner[1], Yuan Cheng[1], Bria M Coates[1,3,4], Hiam Abdala-Valencia[1], Paul A Reyfman[1], Alexander V Misharin[1], GR Scott Budinger[1], Deborah R Winter[2]±, Karen M Ridge[1,5]±

[1]Pulmonary and Critical Care Division [2]Rheumatology Division, Department of Medicine, [3]Department of Pediatrics, Northwestern University Feinberg School of Medicine, Chicago, IL USA, [4]Ann & Robert H. Lurie Children's Hospital of Chicago, Chicago IL, [5]Department of Cell and Molecular Biology, Northwestern University Feinberg School of Medicine, Chicago, IL.

± Contributed equally to this paper

Abstract

Influenza A virus (IAV) infection significantly contributes to global mortality each year. Previous studies have shown that monocyte-derived alveolar macrophages recruited to the lung drive injury during influenza infection. However, the exact timing and mechanism of macrophage-driven lung damage is unknown. Here, we define three distinct patterns of gene expression in recruited macrophages over the first six days post-IAV infection in mice. Additionally, we demonstrate that *Vim*$^{-/-}$ mice infected with IAV exhibit decreased mortality, which was associated with a temporally altered transcriptional response in recruited macrophages. During the early inflammatory phase of IAV response, *Vim*$^{-/-}$ macrophages were characterized by a protective shift in macrophage activation. Furthermore, using a bone-marrow chimera mouse model, we demonstrate that vimentin deficiency in recruited macrophages is sufficient to confer protection from IAV-induced mortality. Taken together, our findings provide new insight into the temporal dynamics of macrophage function in response to IAV infection.

Introduction

Influenza A virus infection is a major contributor to global mortality and morbidity, leading to between ~500,000 deaths globally each year [1]. In 2009, a new strain of H1N1 influenza A virus led to a global pandemic, resulting in an estimated 201,200 respiratory and 83,300 cardiovascular deaths associated with the virus [2]. Influenza infection symptoms include fever, muscle pain and headache, which are the result of a large-scale immune response initiated to clear the virus from the airways and resolve inflammation [3, 4]. While infection in some patients only leads to mild disease and complete recovery, it can cause irreparable lung tissue damage and death in others. This range in severity is thought to correlate with the strength of the immune response, with previous studies demonstrating that hyperactivation of the immune response, resulting in higher pro-inflammatory cytokine production, leads to irreversible lung damage[5-7]. Indeed, both human and mouse studies have demonstrated that higher levels of pro-inflammatory chemokines are correlated with disease severity and could distinguish fatal from non-fatal outcomes[8].

Macrophages are the main cell type in the lung that initiate and orchestrate the immune response after IAV infection [9]. Tissue-resident alveolar macrophages (TR-AM) are the first immune cells to encounter the virus in the lower respiratory tract along with the alveolar epithelium. While important for initiation of the immune response, it has been shown that TR-AM quickly decrease in number upon infection [10-12]. Concurrent with this decrease, monocytes are rapidly recruited from blood into the lung parenchyma where they differentiate into macrophages. Upon extravasation, these Monocyte-derived Alveolar Macrophages (MoAM) secrete an array of pro-inflammatory cytokines and chemokines to induce an immune response and promote recruitment of other immune cells [13]. In some cases, unchecked cytokine and chemokine production can lead to irreversible lung damage and impaired pulmonary function. Our group and others have previously demonstrated that MoAM recruited to the lung drive IAV-induced lung injury [14, 15].

Vimentin, a type III intermediate filament, is ubiquitously expressed in macrophages and is involved in immune response [16]. A few groups have previously suggested a role for vimentin in inflammatory disease such as colitis [17, 18]. Recently, our group demonstrated that in an acute lung injury (ALI) mouse model, vimentin-null mice (*Vim*$^{-/-}$) mice were protected from tissue damage as compared to wild-type control [19]. Specifically, we showed that vimentin is required for NLRP3 inflammasome activation. The NLRP3 inflammasome is central to the innate immunity and to moderating lung pathophysiology in IAV-infected lungs [20, 21]. However, the impact of vimentin-deficiency on macrophage response to IAV infection has not previously been studied.

In this study, we identified three distinct gene expression patterns in macrophages post-IAV infection corresponding to the Infiltrating, Early Inflammatory and Late Inflammatory phases of response. We report that influenza-induced activation of MoAM in the Early Inflammatory phase drives lung injury and mortality in a murine model of viral pneumonia. *Vim*$^{-/-}$ mice demonstrate reduced lung injury and mortality following IAV-infection. MoAM from *Vim*$^{-/-}$ mice exhibited an altered transcriptional response to IAV, particularly in the Early Inflammatory Phase. Using a bone marrow chimera mouse model, we showed that lack of vimentin in recruited MoAM is sufficient to protect WT mice from influenza-induced lung damage and mortality. Taken together, our findings demonstrate that the temporal dynamics of recruited macrophage activation are critical to understanding tissue injury and lethality following influenza infection.

Results

Vim$^{-/-}$ mice are protected from influenza A–induced lung injury

The NLRP3 inflammasome is responsible for initiating the inflammatory response following IAV infection [20, 21]. We previously reported that vimentin is required for the assembly and function of the NLRP3 inflammasome [19]. To investigate whether vimentin-deficiency is protective following IAV infection, wild-type (WT) and *Vim*$^{-/-}$ mice were infected with a lethal dose of IAV (WSN, 200 pfu). WT mice had a 100% mortality rate, whereas <17% of the *Vim*$^{-/-}$ mice died by

10 days post-infection (dpi) (**Figure 1a**). Surviving *Vim*$^{-/-}$ mice exhibited mild lethargy, coat ruffling, febrile shaking, and eye watering but recovered by 14 dpi. IAV infection disrupts basal lung architecture and the alveolar-capillary barrier; therefore, we assessed lung damage in *Vim*$^{-/-}$ mice. Histopathological examination showed that lungs of IAV-infected *Vim*$^{-/-}$ mice had less severe alveolar damage than IAV-infected WT mice, characterized by reduced alveolar edema and cellular infiltrates (**Figure 1b**). Wild-type mice infected with IAV exhibited an increase in total protein concentration in the bronchoalveolar lavage fluid (BALF) and in wet-to-dry lung weight ratio, whereas *Vim*$^{-/-}$ mice failed to exhibit such an increase (**Figure 1c-d**). Vimentin-deficiency did not interfere with IAV replication or clearance as evidenced by comparable viral titers assessed by plaque assay (**Figure 1e**) and similar levels of viral RNA in macrophages (**Supplemental Figure 1a**). These results indicate that, independent of viral load, *Vim*$^{-/-}$ mice have decreased lung injury and improved survival rates following IAV infection.

The influx of immune cells into the airspace during IAV infection and the resulting production of pro-inflammatory cytokines are a major driver of lung injury. To characterize the immune cell recruitment into the lungs, we performed a systematic flow cytometric analysis of whole-lung lysates (**Supplemental figure 1b**). The number of tissue-resident alveolar macrophages (TR-AM) rapidly decreased after IAV infection at a similar rate in both genotypes after accounting for mouse body weight, with a more than 80% reduction by 6 dpi (**Figure 1f**). On the other hand, the monocyte-derived alveolar macrophage (MoAM) population increased over the course of IAV, with *Vim*$^{-/-}$ mice and WT following a similar trend (**Figure 1f**). In addition, the number of neutrophils peaked in both genotypes on day 3 dpi (**Supplemental Figure 1c**). In contrast to the vimentin-independent influx of immune cells following IAV infection, we found that BALF in *Vim*$^{-/-}$ mice had decreased levels of pro-inflammatory cytokines and chemokines, such as IL-1β, TNFα, RANTES, MIP-2 and MCP-1, when compared to WT mice (**Figure 1g**). Although we observe no

change in MoAM numbers in *Vim*$^{-/-}$ mice, the reduction in the inflammatory milieu suggests that there is a change in MoAM function in response to IAV.

The transcriptional response of MoAM to IAV is characterized by three distinct temporal patterns

To investigate the response of MoAM to IAV infection, we performed RNA-seq to assess global gene expression profiles on days 2, 3, 4, and 6 days post-IAV infection (**Supplemental Figure 2a**). We identified 2623 differentially expressed genes over this time course and using k-means clustering, defined three clusters that correspond temporally to phases of IAV response: Infiltrating (2 dpi), Early Inflammatory (3-4 dpi), and Late Inflammatory (6 dpi) (**Figure 2a**).

The first cluster is characterized by genes with highest expression in the **Infiltrating Phase** at 2 dpi (**Figure 2b, Supplemental Figure 2b**). This cluster is enriched for genes such as *Cx3cr1, Rock1, Tln1, and Cxcl14*, associated with the GO processes, *cell migration* and *cell adhesion* (**Figure 2c-d**), which are involved in transendothelial migration of leukocytes [22-25]. These results are consistent with the requirement for MoAM to leave the vasculature and migrate across the endothelium to reach the alveolar space soon after IAV infection. In addition, we also observed genes in this cluster associated with the recruitment of lymphocytes, such as *Cd86,* MHC Class II antigen *H2-Aa,* and *Ccl8* (**Figure 2c,d**). Finally, GO processes associated with proliferating cells, such as *DNA replication initiation*, were also enriched in this cluster (**Figure 2c**). This was further supported by an independent analysis that demonstrated cell cycle genes were expressed at highest levels on 3 dpi and were enriched in this cluster (**Figures 2e-f**). Taken together, these data demonstrate that the primary role of MoAM in the Infiltrating Phase of IAV response is to enter the lung parenchyma, promote the recruitment of immune cells, and proliferate.

The second cluster is characterized by genes that peak in expression during the **Early Inflammatory Phase** at 3 dpi (**Figure 2b, Supplemental Figure 2b**). This cluster is enriched for genes associated with the GO processes, *inflammatory response* and *regulation of cytokine secretion* (**Figure 2c)** – such as *Tlr2*, *Il1a*, *Il1b,* and *Il1r2* **(Figure 2d)**. This is consistent with the transition of MoAM from infiltrating the parenchyma to binding viral PAMPs through pattern recognition receptors (PRRs), including TLR2, and initiating production of pro-inflammatory molecules [26]. The expression patterns of *Ccl2* and *Cxcl2,* which are involved in the enriched GO process *neutrophil chemotaxis* (**Figure 2c-d**), corresponded with the highest secretion of their respective proteins MCP-1 and MIP-2 measured on 3 dpi in BALF (**Figure 1g**). These data are also in line with the peak in neutrophil infiltration into the lung at 3 dpi (**Supplemental Figure 1b**). Collectively, these data demonstrate that MoAM adopt a pro-inflammatory activation during the Early Inflammatory Phase of IAV response.

The third cluster is characterized by genes that display a continuous increase in expression until the **Late Inflammatory Phase** at 6 dpi (**Figure 2b, Supplemental Figure 2b**). This cluster is enriched for genes associated with the GO processes *cell differentiation* and *adaptive immune response* – such as *Ccr1, Arg2, Ctsh,* and *Ifng* (**Figure 2d, Supplemental Figure 2c)**. After the peak of inflammation, MoAM must transition into a more stable phenotype [27]. As a part of this process, we found that this cluster was enriched for genes involved in monocyte differentiation and macrophage maturation, such *Irf8* and *Mafb* [28, 29] (**Figure 2d**). Since GO analysis implicated metabolic processes in this cluster (**Figure 2c**) and macrophage activation has been associated with changes in cellular respiration [30-32], we investigated whether glycolysis and oxidative phosphorylation were altered during this phase. We did not observe preferential expression of associated genes at any timepoint and neither pathway showed enrichment across phases (**Figure 2f**). Interestingly, the gene encoding vimentin was included in this cluster, suggesting that it may play a role throughout IAV response (**Figure 2c**). Overall, these data

demonstrate that MoAM adopt a more mature phenotype during the Late Inflammatory Phase of IAV response.

Macrophage responses are commonly categorized as either pro-inflammatory or alternative activation. Although many studies have shown that activated macrophages actually form a much wider spectrum, LPS/IFNγ and IL-4 are often used as typical stimuli representing pro-inflammatory and alternative activation, respectively [33-35]. Thus, we generated annotations for these responses by integrating the gene sets resulting from several published studies on LPS/IFNy ($M_{(LPS/IFN\gamma)}$ -pro-inflammatory) and IL-4 ($M_{(IL-4)}$-alternative) stimulation in macrophages (Methods). We found that genes associated with $M_{(LPS/IFN\gamma)}$ peaked in expression on 3 dpi **(Figure 2e),** and were enriched in the early and late inflammatory phases (**Figure 2f**). Furthermore, we found that genes associated with $M_{(IL-4)}$ peaked on 2 dpi and were enriched in the Infiltrating phase (**Figure 2e-f)**. Thus, MoAM exhibit distinct functions during each of the three phases of IAV response.

Vim$^{-/-}$ MoAM have an altered transcriptional response to IAV

To gain a better understanding of the conferred protection from IAV infection in *Vim*$^{-/-}$ mice (**Figure 1**), we performed RNA-seq on MoAM isolated from *Vim*$^{-/-}$ mice at days 2, 3, 4 and 6 following IAV infection (**Supplemental Figure 3a**). Using the prior clustering of 2623 genes across the three phases of IAV response (**Figure 2a**), we compared expression between MoAMs in WT and *Vim*$^{-/-}$ mice (**Figure 3a**). On average, we found that expression of genes in the Infiltrating cluster were higher in *Vim*$^{-/-}$ MoAM than WT: this difference was most pronounced at 3dpi (**Figure 3b**, **Supplemental Figure 3b**). Genes in the Early Inflammatory cluster generally exhibited lower levels of expression in *Vim*$^{-/-}$ MoAM compared to WT: again, the largest difference between genotypes was observed at 3dpi (**Figure 3b, Supplemental Figure 3b**). In contrast, genes in the

Late Inflammatory cluster demonstrated less significant changes on average between genotypes (**Figure 3b, Supplemental Figure 3b**).

To compare the number of genes that were altered over the course of IAV response in each cluster, we set a cutoff on the overall difference, calculated by Euclidean distance, between WT and *Vim*$^{-/-}$ mice (**Figure 3c**). We found that the Infiltrating cluster contained the most genes with altered expression (45%) compared with Early (29%) and Late (21%) Inflammatory clusters (**Figure 3d**). These altered genes were associated with the GO processes, *DNA replication* (*p-value =7.55 x* 10^{-4}) and *regulation of chromosome organization (p-value=5.44 x*10^{-6}*)*, suggesting that these functions differ in the response of *Vim*$^{-/-}$ MoAM to IAV infection. The low proportion of altered genes across time in the Early Inflammatory cluster is likely due to disproportionate number of differential genes on 3 and 4dpi (**Supplemental Figure 3c)**. The changes between WT and *Vim*$^{-/-}$ MoAM on 3 dpi may result from the fact that the *Vim*$^{-/-}$ cells do not undergo the shift in gene expression observed in WT from 2 to 3dpi (**Supplemental Figure 3d).** Taken together, these data suggest that vimentin-deficiency has the greatest impact on MoAM function in IAV response during the transition to the Early Inflammatory phase.

Vim$^{-/-}$ MoAM downregulate $\mathbf{M_{(LPS/IFN\gamma)}}$ gene expression over the course of IAV

We previously showed that genes associated with pro-inflammatory response ($\mathbf{M_{(LPS/IFN\gamma)}}$) were expressed in MoAM during the Early and Late Inflammatory phases following IAV infection (**Figure 2h**). In MoAM from *Vim*$^{-/-}$ mice, these genes did not exhibit a comparable increase in expression (**Figure 4a**). As a group, these genes were significantly down-regulated in MoAM from *Vim*$^{-/-}$ mice during the course of IAV response but there was no difference in expression of these genes in baseline alveolar macrophages (TR-AM, **Supplemental Figure 4a**). Moreover, Gene Set Enrichment Analysis (GSEA) revealed significant negative enrichment of $M_{(LPS/IFN\gamma)}$

genes on 2,3 and 6 dpi in *Vim*$^{-/-}$ MoAM (**Figure 4b**). When comparing the most down-regulated **M**$_{(LPS/IFN\gamma)}$ genes from each dpi (the GSEA leading edge), we found that 27 out of 84 genes were found on all days (**Figure 4c-d**, **Supplemental Figure 4b**). The observed decrease in pro-inflammatory genes, which were associated with the Early Inflammatory phase, suggest that *Vim*$^{-/-}$ MoAM adopt a more protective, dampened pro-inflammatory signature in response to IAV.

Vim$^{-/-}$ MoAM upregulate expression of cell cycle and M$_{(IL-4)}$ genes

To further investigate the changes in macrophage function in *Vim*$^{-/-}$ MoAM, we compared the expression of genes in processes associated with the Infiltrating phase of IAV response (**Figure 2h**). We found that genes involved in *Cell Cycle* and *M*$_{(IL-4)}$ were more highly expressed in *Vim*$^{-/-}$ compared to WT MoAM over all days post-infection (**Figure 5a, Supplemental Figure 5a**). Both *Cell Cycle* and *M*$_{(IL-4)}$ associated genes exhibited fairly constant expression in *Vim*$^{-/-}$ MoAM over time, while these genes decreased in expression in WT MoAM. Neither sets of genes were significantly different in baseline alveolar macrophages (TR-AM, **Supplemental Figure 5a**). GSEA demonstrated that both *M*$_{(IL-4)}$ *response* and *Cell Cycle* were significantly enriched among genes that were increased in expression in the *Vim*$^{-/-}$ MoAM during the entire IAV response (**Figure 5b, Supplemental Figure 5b)**. Taken together, these data suggest that *Vim*$^{-/-}$ MoAM do not exhibit the decrease in alternative activation (*M*$_{(IL-4)}$) or proliferation typically observed in the Early Inflammatory phase of IAV response.

Vimentin-deficient MoAM are sufficient to confer protection from IAV-induced mortality

To determine whether vimentin-deficiency in recruited macrophages alone could decrease lung injury following IAV infection, we generated bone marrow chimeras with mixed WT *or Vim*$^{-/-}$ genotypes. Bone marrow from either WT donor mice (CD45.2) or *Vim*$^{-/-}$ donor mice (CD45.2) were transferred into irradiated WT recipient mice (CD45.1), allowing for the specific reconstitution

of MoAM with a WT or *Vim*$^{-/-}$ genotype (**Figure 6a**). All mice showed reconstitution of donor hematopoietic cells in peripheral blood above 85% genotype (**Supplementary Figure 6a**). Following confirmed engraftment and recovery, mice were infected with a lethal dose of IAV (**Figure 6a**). We found that IAV-infected WT mice who received *Vim*$^{-/-}$ donor bone marrow exhibited significantly lower total protein concentration in the BALF and lower wet-to-dry lung weight ratio compared to those who received WT donor bone marrow, indicating less severe alveolar damage (**Figure 6b-c**). Mice showed no difference in IAV replication or clearance regardless of donor genotype (**Figure 6d**). As in *Vim*$^{-/-}$ mice (**Figure 1**), WT mice with *Vim*$^{-/-}$ MoAM exhibited lower levels of pro-inflammatory cytokines and chemokines (**Figure 6e**). Taken together, these data support the role of MoAM in effecting the protective function of vimentin-deficiency in response to IAV. Thus, it follows that MoAM drive lung injury following IAV infection.

Discussion

Our data demonstrated that vimentin-deficiency confers protection from lung damage and mortality following IAV infection through altering MoAM activation during the Early Inflammatory phase of response. We also characterized the time course by which macrophages respond to IAV infection. Previous studies have compared macrophages at baseline and following IAV infection[9, 36, 37]. However, our results suggest that macrophages engage in different functions depending on the phase of IAV response. Thus, it would be impossible to understand how macrophages contribute to lung injury without investigating them at multiple time points. Through transcriptional profiling, we were able to identify novel macrophage functions following IAV response and place them, as well as canonical processes, in their appropriate temporal context. These included cell cycle, pro-inflammatory, and metabolic functions, which we categorized into Infiltrating, Early Inflammatory, and Late Inflammatory, respectively. Our timeline was restricted to the first few days post-infections. Future studies could expand on our data by connecting our

results to circulating monocytes and alveolar macrophages at baseline or the prolonged response of recruited macrophages as mice recover from IAV [38].

The *Vim*$^{-/-}$ mouse has provided insights into the functions of vimentin in the inflammatory response to influenza A virus infection. Under normal conditions vimentin is known to play an important role in coordinating the activation of signaling pathways known to regulate inflammatory mediator levels in resident tissue cells and in inflammatory cells recruited from the blood[39]. Vimentin has been implicated as a source of structural support in lymphocytes. This structural support is thought to limit mechanical deformations of lymphocytes following chemokine-induced polarization [40]. In related morphological studies of circulating lymphocytes in normal mice there is a pronounced reorganization of vimentin intermediate filament networks and this reorganization is associated with extravasation [41]. The *Vim*$^{-/-}$ mouse has also provided important insights into the role of vimentin in regulating the activation of the NLRP3 inflammasome. The inflammasome is a large multiprotein complex, which plays a key role in innate immunity by regulating the production of the pro-inflammatory cytokines. Pro- interleukin-1β (IL-1β) and pro-IL-18 require caspase-1 to produce the mature and active forms of IL-1β and IL-18. These cytokines cause a wide variety of biological effects associated with infection, inflammation and autoimmune processes. Influenza A virus and LPS are known activators of the NLRP3 inflammasome[42]. *Vim*$^{-/-}$ mice are protected from LPS-induced injury and have reduced IL-1β levels [19]. Furthermore, disruption of normal vimentin intermediate filament organization in macrophages by using withaferin A abrogates the formation of NLRP3 inflammasomes [19, 44]. In agreement, vimentin have been shown to interact with macrophage-inhibitory factor (MIF), which is required for NLRP3 inflammasome activation [44]. Taken together, these studies and this report demonstrate that vimentin contributes to the host innate immune response system. Innate and adaptive immune responses are necessary for the successful clearance of pathogens, but an excessive immune response (e.g. release of pro-inflammatory

cytokines) can induce tissue damage. The above studies demonstrate a proof of principle that disrupting vimentin is a translationally relevant approach to modulating the inflammatory response and protecting the host.

Understanding the function of MoAM in IAV response is critical to the future development of treatments that decrease lung damage and mortality. Enhancing or dampening macrophage function may be key to improving outcomes post-IAV infection. Changes to macrophage function in the young and elderly may explain why they experience increased IAV-associated mortality. In addition to driving inflammatory responses, macrophages are also responsive to changes in their environment. Thus, transcriptional profiling of macrophages may also reveal how other lung cells, such alveolar epithelial cells, are impacted by IAV infection. Exploring the interactions between cell types in response to IAV may provide further insight into the underlying mechanisms. Further investigation of the role of macrophages in IAV response is necessary to better understand how they might be used a therapeutic target.

Materials & Methods

Mice. All experiments were performed using wild-type or vimentin-null (*Vim*$^{-/-}$) 129S/V mice, age 8-12 weeks. Wild-type mice were purchased from Taconic, *Vim*$^{-/-}$ mice were a gift from Albee Messing (University of Wisconsin, Madison, WI). All animals were kept under pathogen-free conditions, and all experiments were approved in accordance with Northwestern University's Institutional Animal Care and Use Committee (IACUC) guidelines.

Bone marrow chimeras. 8-12 week old recipient mice (Ptprc^{a}/Pep-Boy, CD45.1) were lethally irradiated with a single dose of 1,000 cGy γ-radiation using a Cs-137–based Gammacell-40 irradiator (Nordion). Within 24 hours, fresh bone marrow cells (2 x 10^{6}) from either WT donor mice or *Vim*$^{-/-}$ donor mice (CD45.2) were injected via retro-orbital injection. Mice were housed together in individually ventilated cages and were given *ad libitum* access to food and water supplemented

with Trimetoprim/Sulfamethoxazole (TMP/SMX 40/8 mg formula, Hi-Tech Pharmacal) for 4 weeks and then switched to normal housing regimen. Reconstituted mice were used for influenza infection experiments ~4 weeks after transplantation. Engraftment was assessed after two weeks, using flow cytometry to measure percentage of CD45.1+ and CD45.2+ cells in peripheral blood collected from the facial vein. All mice used for experiments showed reconstitution of donor (CD45.2) circulating leukocytes in peripheral blood above 85%.

Virus. H1N1 Influenza virus strain A/WSN/1933 (WSN) was propagated in fertile chicken eggs (Sunnyside Hatchery) as previously described [15]. Viral titers were determined by measurement of plaque-forming units (pfu) in Madin-Darby canine kidney epithelial cells (ATCC).

Plaque Assay. Confluent monolayers of Madin-Darby canine kidney epithelial cells were infected with stock WSN virus in 1% BSA DMEM for 2h at 37°C. Plates were washed with PBS and an overlay of 50% 2x replacement media (2x DMEM, 0.12M $NaHCO_3$, 2% penicillin-streptomycin, and 1% HEPES), 50% Avicel (2.35%), and N-acetyl trypsin (1.5μg/mL) remained on the cells for 72h at 37°C. Plates were washed with PBS and fixed with 0.2% PFA before staining the monolayers with naphthalene blue-black stain.

In vivo influenza virus infection. 8-12 week old WT and *Vim*$^{-/-}$ 129S/V male mice were anesthetized using isoflurane and intratracheally (i.t.) infected with 200 pfu WSN. Mice were monitored daily and weight was recorded every 24 hours.

Histology. Mice were euthanized after which a 20-gauge angiocath was sutured into the trachea. Heart and lungs were removed *en bloc*, and lungs were inflated with 0.8mL of 4% paraformaldehyde (PFA) at a pressure not exceeding 16 cm H_2O. Tissue was fixed and embedded in paraffin. 5 μm sections were stained with H&E by the Mouse Histology Phenotyping Laboratory (Northwestern University, Chicago, IL). Tissue sections were visualized using TissueGnostics, a Tissue/Cell High Throughput Imaging Analysis Systems (Vienna, Austria) and

captures using TissueFAXS software (TissueGnostics, Los Angeles, CA) at the Northwestern University Cell Imaging Facility (Northwestern University, Chicago, IL).

Bronchoalveolar Lavage. A 20-gauge angiocath was ligated into the trachea and 1mL of sterile PBS instilled into the lungs, then removed through the angiocath. This process was repeated three times. Bronchoalveolar lavage fluid (BALF) was centrifuged at 500 x *g* for 10 min. Protein levels in supernatant were measured by Bradford assay (Bio-Rad) and cytokine levels were measured using a custom multiplex ELISA (ThermoFisher Scientific).

Wet-to-dry weight ratio. Mice were euthanized and lungs were surgically removed *en bloc*. The left lung was ligated, excised, and weighed in a tared container. Left lung was dried at 70°C in a Speed-Vac SC100 evaporator (Thermo Scientific, Waltham, MA) until a constant weight was obtained, and the wet-to-dry weight ratio was calculated.

***Flow cytometry analysis of lung cell populations*.** Mice were euthanized and lungs were perfused with 10mL HBSS with Ca^{2+} and Mg^{2+}. Lung loves were removed and inflated with enzyme solution (5mL of 0.2 mg/mL DNase I and 2 mg/mL collagenase D in HBSS with Ca^{2+} and Mg^{2+}) using a 30-gauge needle. Tissue was minced and processed in gentleMACS dissociator tubes according to manufacturer's instructions (Miltenyi Biotec). Processed lungs were passed through a 40μm cell strained, and RBCs were lysed using BD PharmLyse (BD Biosciences, San Jose, CA). Remaining cells were counted using a Countess cell counter (Invitrogen, Grand Island, NY). CD45 microbeads were added and cells were eluted according to Miltenyi manufacturer's instructions. Cells were stained with viability dye Aqua (Invitrogen) and non-specific antibody (Ab) binding was inhibited by adding Fc Block (553142, clone 2.4G2; BD Pharmingen). Blocked cells were stained with a mixture of fluorochrome-conjugated Abs (see **Online Supplemental Table 1** for list of Abs). Data were acquired on a BD LSR II flow cytometer using BD FACSDiva software (BD Biosciences), and data analyses were performed using FlowJo software (Tree Star, Ashland,

OR). Cell populations were identified using sequential gating strategy (**Supplemental Figure 1b)**. Cell number was normalized to body weight.

Macrophage harvesting and flow sort. Mice were euthanized, and perfused with 5 mL sterile PBS by cardiac perfusion through the right ventricle. A 20-gauge angiocath was ligated into the trachea and lung and trachea were removed *en bloc*. Lungs were instilled with 1 mL dispase (Corning) through the angiocath, and a second suture was tied around the trachea to avoid leakage. Lungs were placed in 50 mL tubes (Falcon) containing 750 μL cold dispase and rocked for 45 min. at RT. Trachea and angiocath were removed, and lungs were minced using curved-edge scissors. Digested tissue was poured into 50 mL tubes containing 7 mL DMEM (Corning) and 14 μL DNase I (50 mg/mL, Sigma). Tubes were rocked for 10 minutes at RT. Using serological pipettes, tissue was gently further disrupted, and subsequently filtered through 70 μm cell strainers and 40 μm strainers (Corning). Tubes were rinsed with DMEM + 5% FBS and filtered through the same strainers. Cell suspensions were centrifuged for 10 min. at 1300 rpm, 4°C, and pellets were resuspended in 350 μL MACS buffer (Milteny). 100 μL CD11c magnetic microbeads (Milteny) were added and cells were eluted according to Miltenyi manufacturer's instructions. Cells were stained for CD11b (Biolegend), Siglec F (BD), Ly6C (eBioscience), CD45 (eBioscience), MHCII (Biolegend), CD64 (Biolegend), Ly6G (BD), and NK1.1(BD). Viability dye (eFluor506, eBioscience) was used to sort living cells only (**Online Supplemental Table 1**). Using sequential gating (**Online Supplemental Figure 1),** recruited alveolar macrophages (MoAM) and tissue-resident alveolar macrophages (TR-AM) were flow sorted using a BD FACSaria III 5-laser cell sorter and 100 μm nozzle (BD Biosciences). Flow-sorted cells were collected into 1.5 mL Eppendorf tubes containing 200 μL MACS buffer, and centrifuged at 5,000 rpm for 5 min. at RT. Pellets were resuspended and lysed in RLT lysis buffer (Qiagen) and stored at -80°C until all time points were collected.

RNA sequencing (RNA-seq). To minimize batch effect, all samples belonging to a cell type were thawed at the same time for RNA isolation. All libraries for a given cell type were prepared as a single batch for sequencing. Total RNA was isolated using RNeasy Plus Mini kits (Qiagen). RNA quality (RIN) and quantity were assessed using a TapeStation 4200 (Agilent Technologies). RIN scores ranged from 7.2 to 9.4, with an average of 8.6. Using poly(A) mRNA magnetic enrichment kits from NEBNext (New England Biolabs), mRNA was isolated. cDNA libraries were prepared using NEBNext Ultra DNA library kits (New England BioLabs) for Illumina. Libraries were sequenced using high-output 75-cycle single-end kits on an Illumina NextSeq 500 sequencer. Reads were demultiplexed (bcl2fastq), trimmed, and aligned to reference genome mm10 using TopHat2 [45]. Aligned reads were mapped to genes using HTSeq with an Ensembl annotation[46].

RNA-seq analysis

Expression data tables used were normalized FPKM counts. Low counts were removed, with a cut-off set as row sum > n(# of libraries used for analysis). For pairwise comparison, low counts were trimmed if CPM <2 in x number of replicates, x being the number of replicates in the smallest group of the comparison. Differential gene expression was assessed by pairwise comparison between two groups (edgeR) [47, 48] and one-way ANOVA with Benjamini-Hochberg (BH) correction, for comparison between more than two groups. Clustering was performed using k-means clustering (GENE-E, https://software.broadinstitute.org/GENE-E/index.html). Euclidean distance values (d) were calculated between *Vim*$^{-/-}$ and WT z-score values. Output for each gene was a single Euclidean distance value (d), and distribution of d for all genes for each phase were plotted using ggplot2 in R. PCA plots were generated using DeSeq2 [49]. Pearson correlation matrix and heatmaps were generated using GENE-E. Gene ontology (GO) term association for clusters was run using GOrilla [50, 51]. Gene set enrichment analysis (GSEA) was run on pre-

ranked log_2FC edgeR output data using GSEA [52, 53]. Overlaps between gene lists were visualized using Venny (https://bioinfogp.cnb.csic.es/tools/venny/index.html).

Custom gene set generation. Custom gene sets for LPS/IFNγ and IL-4 stimulated were generated by querying primary published data available in relevant experimental models. The final curated gene sets, $M_{(LPS/IFN\gamma)}$ and $M_{(IL\text{-}4)}$, were derived from four primary publications[33-35, 54]. All four publications used mouse bone-marrow derived macrophages (BMDM), and stimulated them *in vitro* with either LPS+IFNγ, or IL-4. Methodologies used included LC-ESI-MS/MS mass spectrometry, microarray, and RNA-seq. A summary of experimental approach, methods, and results for all publications can be found in **Online Supplemental Table 2**. After gene names were annotated with Ensembl IDs, any genes without an Ensembl ID associated were removed. Three genes were found in both gene sets, and were removed to avoid any overlap between gene sets. These trimming steps resulted in two annotated gene set lists, 110 LPS/IFNγ stimulated genes, and 101 IL-4 stimulated genes (**Online Supplemental Table 2**).

***Viral reads*.** To identify viral reads within libraries, unmapped reads were aligned to H1N1 reference genome. Reads for the H1N1 matrix protein 2 (M2), nucleoprotein (NP), and neuraminidase (NA) were normalized to number of uniquely aligned (mm10) reads.

Statistics. Analyses for cytokine levels, BALF protein, viral titer, and wet-to-dry ratio were performed using GraphPad Prism (GraphPad Software). Enrichment of processes (**Figure 2h**) was calculated using hypergeometric testing.

Acknowledgments

We thank Jennifer Davis for acquiring and processing microscopic images in Figure 1. Histology services were provided by the Northwestern University Mouse Histology and Phenotyping Laboratory which is supported by NCI P30-CA060553 awarded to the Robert H Lurie

Comprehensive Cancer Center. Flow Cytometry was supported by the Northwestern University Flow Cytometry Facility. Graphic design was created with BioRender.com

References

1. Kilbourne, E.D., *Influenza pandemics of the 20th century.* 2006. **12**(1): p. 9-14.
2. Dawood, F.S., et al., *Estimated global mortality associated with the first 12 months of 2009 pandemic influenza A H1N1 virus circulation: a modelling study.* 2012. **12**(9): p. 687-95.
3. Eccles, R., *Understanding the symptoms of the common cold and influenza.* The Lancet Infectious Diseases, 2005. **5**(11): p. 718-25.
4. Monto, A.S., et al., *Clinical signs and symptoms predicting influenza infection.* Arch Intern Med, 2000. **160**(21): p. 3243-7.
5. Hayden, F.G., et al., *Local and systemic cytokine responses during experimental human influenza A virus infection. Relation to symptom formation and host defense.* J Clin Invest, 1998. **101**(3): p. 643-9.
6. Davidson, S., et al., *Pathogenic potential of interferon alphabeta in acute influenza infection.* Nat Commun, 2014. **5**: p. 3864.
7. Teijaro, J.R., et al., *Mapping the innate signaling cascade essential for cytokine storm during influenza virus infection.* Proc Natl Acad Sci U S A, 2014. **111**(10): p. 3799-804.
8. de Jong, M.D., et al., *Fatal outcome of human influenza A (H5N1) is associated with high viral load and hypercytokinemia.* Nature Medicine, 2006. **12**(10): p. 1203-7.
9. Tate, M.D., et al., *Critical role of airway macrophages in modulating disease severity during influenza virus infection of mice.* Journal of Virology, 2010. **84**(15): p. 7569-80.
10. Brown, A.S., et al., *Cooperation between Monocyte-Derived Cells and Lymphoid Cells in the Acute Response to a Bacterial Lung Pathogen.* PLoS Pathog, 2016. **12**(6): p. e1005691.
11. Hashimoto, D., et al., *Tissue-resident macrophages self-maintain locally throughout adult life with minimal contribution from circulating monocytes.* Immunity, 2013. **38**(4): p. 792-804.
12. Ghoneim, H.E., P.G. Thomas, and J.A. McCullers, *Depletion of alveolar macrophages during influenza infection facilitates bacterial superinfections.* J Immunol, 2013. **191**(3): p. 1250-9.
13. Pirhonen, J., et al., *Virus infection activates IL-1 beta and IL-18 production in human macrophages by a caspase-1-dependent pathway.* Journal of Immunology, 1999. **162**(12): p. 7322-9.
14. Lin, K.L., et al., *CCR2+ monocyte-derived dendritic cells and exudate macrophages produce influenza-induced pulmonary immune pathology and mortality.* J Immunol, 2008. **180**(4): p. 2562-72.
15. Coates, B.M., et al., *Inflammatory Monocytes Drive Influenza A Virus-Mediated Lung Injury in Juvenile Mice.* J Immunol, 2018. **200**(7): p. 2391-2404.
16. Herrmann, H., et al., *Structure and assembly properties of the intermediate filament protein vimentin: the role of its head, rod and tail domains.* J Mol Biol, 1996. **264**(5): p. 933-53.
17. Mor-Vaknin, N., et al., *Murine colitis is mediated by vimentin.* Sci Rep, 2013. **3**: p. 1045.
18. Henderson, P., et al., *A role for vimentin in Crohn disease.* Autophagy, 2012. **8**(11): p. 1695-6.
19. dos Santos, G., et al., *Vimentin regulates activation of the NLRP3 inflammasome.* Nat Commun, 2015. **6**: p. 6574.
20. Allen, I.C., et al., *The NLRP3 inflammasome mediates in vivo innate immunity to influenza A virus through recognition of viral RNA.* Immunity, 2009. **30**(4): p. 556-65.

21. Thomas, P.G., et al., *The intracellular sensor NLRP3 mediates key innate and healing responses to influenza A virus via the regulation of caspase-1.* Immunity, 2009. **30**(4): p. 566-75.
22. Imai, T., et al., *Identification and molecular characterization of fractalkine receptor CX3CR1, which mediates both leukocyte migration and adhesion.* Cell, 1997. **91**(4): p. 521-30.
23. Worthylake, R.A. and K. Burridge, *RhoA and ROCK promote migration by limiting membrane protrusions.* Journal of Biological Chemistry, 2003. **278**(15): p. 13578-84.
24. Lammermann, T., et al., *Rapid leukocyte migration by integrin-independent flowing and squeezing.* Nature, 2008. **453**(7191): p. 51-5.
25. Starnes, T., et al., *The chemokine CXCL14 (BRAK) stimulates activated NK cell migration: implications for the downregulation of CXCL14 in malignancy.* Experimental Hematology, 2006. **34**(8): p. 1101-5.
26. Mogensen, T.H., *Pathogen recognition and inflammatory signaling in innate immune defenses.* Clinical Microbiology Reviews, 2009. **22**(2): p. 240-73.
27. Kratofil, R.M., P. Kubes, and J.F. Deniset, *Monocyte Conversion During Inflammation and Injury.* 2017. **37**(1): p. 35-42.
28. Kelly, L.M., et al., *MafB is an inducer of monocytic differentiation.* EMBO Journal, 2000. **19**(9): p. 1987-97.
29. Hagemeyer, N., et al., *Transcriptome-based profiling of yolk sac-derived macrophages reveals a role for Irf8 in macrophage maturation.* 2016. **35**(16): p. 1730-44.
30. Sanchez, K.K., et al., *Cooperative Metabolic Adaptations in the Host Can Favor Asymptomatic Infection and Select for Attenuated Virulence in an Enteric Pathogen.* 2018. **175**(1): p. 146-158.e15.
31. Smallwood, H.S., et al., *Targeting Metabolic Reprogramming by Influenza Infection for Therapeutic Intervention.* Cell Reports, 2017. **19**(8): p. 1640-1653.
32. Singer, B.D. and N.S. Chandel, *Immunometabolism of pro-repair cells.* 2019. **129**(7): p. 2597-2607.
33. Jablonski, K.A., et al., *Novel Markers to Delineate Murine M1 and M2 Macrophages.* PLoS One, 2015. **10**(12): p. e0145342.
34. Hans, C.P., et al., *Transcriptomics Analysis Reveals New Insights into the Roles of Notch1 Signaling on Macrophage Polarization.* 2019. **9**(1): p. 7999.
35. Gensel, J.C., et al., *Predictive screening of M1 and M2 macrophages reveals the immunomodulatory effectiveness of post spinal cord injury azithromycin treatment.* Sci Rep, 2017. **7**: p. 40144.
36. Zhang, J., et al., *Two waves of pro-inflammatory factors are released during the influenza A virus (IAV)-driven pulmonary immunopathogenesis.* 2020. **16**(2): p. e1008334.
37. Aegerter, H., et al., *Influenza-induced monocyte-derived alveolar macrophages confer prolonged antibacterial protection.* 2020. **21**(2): p. 145-157.
38. Misharin, A.V., et al., *Monocyte-derived alveolar macrophages drive lung fibrosis and persist in the lung over the life span.* Journal of Experimental Medicine, 2017. **214**(8): p. 2387-2404.
39. Cheng, F. and J.E. Eriksson, *Intermediate Filaments and the Regulation of Cell Motility during Regeneration and Wound Healing.* Cold Spring Harbor perspectives in biology, 2017

.

40. Barberis, L., et al., *Leukocyte transmigration is modulated by chemokine-mediated PI3Kgamma-dependent phosphorylation of vimentin.* Eur J Immunol, 2009. **39**(4): p. 1136-46.
41. Brown, M.J., et al., *Rigidity of circulating lymphocytes is primarily conferred by vimentin intermediate filaments.* J Immunol, 2001. **166**(11): p. 6640-6.

42. dos Santos, G., M.A. Kutuzov, and K.M. Ridge, *The inflammasome in lung diseases.* Am J Physiol Lung Cell Mol Physiol, 2012. **303**(8): p. L627-33.
43. Grin, B., et al., *Withaferin a alters intermediate filament organization, cell shape and behavior.* PLoS ONE [Electronic Resource], 2012. **7**(6): p. e39065.
44. Lang, T., et al., *Macrophage migration inhibitory factor is required for NLRP3 inflammasome activation.* Nat Commun, 2018. **9**(1): p. 2223.
45. Kim, D., et al., *TopHat2: accurate alignment of transcriptomes in the presence of insertions, deletions and gene fusions.* 2013. **14**(4): p. R36.
46. Anders, S., P.T. Pyl, and W. Huber, *HTSeq--a Python framework to work with high-throughput sequencing data.* Bioinformatics, 2015. **31**(2): p. 166-9.
47. Robinson, M.D., D.J. McCarthy, and G.K. Smyth, *edgeR: a Bioconductor package for differential expression analysis of digital gene expression data.* Bioinformatics, 2010. **26**(1): p. 139-40.
48. McCarthy, D.J., Y. Chen, and G.K. Smyth, *Differential expression analysis of multifactor RNA-Seq experiments with respect to biological variation.* Nucleic Acids Res, 2012. **40**(10): p. 4288-97.
49. Love, M.I., W. Huber, and S. Anders, *Moderated estimation of fold change and dispersion for RNA-seq data with DESeq2.* Genome Biology, 2014. **15**(12): p. 550.
50. Eden, E., et al., *Discovering motifs in ranked lists of DNA sequences.* PLoS Comput Biol, 2007. **3**(3): p. e39.
51. Eden, E., et al., *GOrilla: a tool for discovery and visualization of enriched GO terms in ranked gene lists.* BMC Bioinformatics, 2009. **10**: p. 48.
52. Mootha, V.K., et al., *PGC-1alpha-responsive genes involved in oxidative phosphorylation are coordinately downregulated in human diabetes.* 2003. **34**(3): p. 267-73.
53. Subramanian, A., et al., *Gene set enrichment analysis: a knowledge-based approach for interpreting genome-wide expression profiles.* Proc Natl Acad Sci U S A, 2005. **102**(43): p. 15545-50.
54. Becker, L., et al., *Unique proteomic signatures distinguish macrophages and dendritic cells.* PLoS ONE [Electronic Resource], 2012. **7**(3): p. e33297.

Figure legends

Figure 1. Vimentin-null mice are protected from influenza-induced lung injury and mortality.

a) Survival of wild-type (WT) and *Vim*$^{-/-}$ mice intratracheally infected with influenza A virus (IAV) (200pfu). WT mice had a 100% mortality rate, whereas only 17% of *Vim*$^{-/-}$ mice died by day 10 post-infection (p.i.). Data shown are n=12 per group. **b)** Representative images of murine lung architecture assessed by H&E staining, scale bar 100 μm. At steady state, basal lung architecture was similar in WT and *Vim*$^{-/-}$ mice. At day 7 p.i., WT lungs exhibited more histologic evidence of lung injury and cellular infiltration compared to *Vim*$^{-/-}$ animals. **c)** *Vim*$^{-/-}$ mice had less protein in bronchoalveolar lavage fluid (BALF), n=5/timepoint. **d)** WT lungs have a greater wet/dry ratio at day 7 p.i. **e)** Viral titers were unchanged between WT and *Vim*$^{-/-}$ mice. **f)** Flow cytometric analysis demonstrated that *Vim*$^{-/-}$ mice had similar numbers of tissue resident (TR-AM) and infiltrating monocyte-derived alveolar macrophages (MoAM) out of the total lung CD45+ cell population normalized to body weight during the IAV response **g)** *Vim*$^{-/-}$ mice had lower levels of inflammatory cytokines in BALF compared with WT mice post-IAV infection, n=4/timepoint. Bar graphs represent mean, error bars represent SD.

Supplemental Figure 1. a) Quantification of H1N1 viral RNA molecules detected among RNA isolated from monocyte-derived macrophages (MoAM), normalized to the number of reads uniquely aligned to mouse (mm10). Bar graphs represent mean, error bars represent SD. **b)** Gating strategy used for flow cytometry analysis of neutrophils, tissue-resident alveolar macrophages (TR-AM) and MoAM. **c)** Flow cytometric analysis demonstrated no differences in number of neutrophils out of the total lung CD45+ cell population normalized to body weight between *Vim*$^{-/-}$ and WT mice during the IAV response.

Figure 2. Wild-type monocyte-derived alveolar macrophages have a distinct temporal transcriptional response to Influenza A viral infection.

a) Heatmap of normalized expression of 2623 differentially expressed genes (ANOVA adjusted p-value <0.05). Z-score normalization for each row was applied to FPKM data. K-means clustering (k=3) identified three clusters; Infiltrating (1131), Early Inflammatory (440), Late Inflammatory (1052). **b)** Mean z-scores calculated across genes for each cluster **c)** GO term enrichment for each phase. Gene ratio represents genes present in each phase for each given term divided by the total number of genes in the term. **d)** Bar graphs of FPKM expression for representative genes in each phase. Error bars represent SD. **e)** Bubble plot representing the proportion of genes (%) within each process that had an expression above the row mean. Color gradient represents mean z-score of expression across genes. **f)** Enrichment of gene sets in each cluster as defined in A. Asterisk represents significantly enriched overlaps (hypergeometric p-value <0.05). (n=3-4 per group). Ox Phos = Oxidative phosphorylation.

Supplemental Figure 2. a) Schematic of experimental design and work flow. WT or *Vim*$^{-/-}$ mice were infected with a lethal dose of influenza virus (200 pfu). MoAM were sorted by flow from lungs on 2,3,4 and 6 dpi. Total RNA was isolated, mRNA was enriched, and bulk RNA-seq was performed and principal component analysis (PCA) performed to visualize replicates. **b)** Violin plots of log2(FPKM+1) counts data, for all genes in each cluster. Solid lines represent median, dotted lines represent quartiles. **c)** Bar graphs of FPKM expression for Arg2 expressed in the Late Inflammatory phase.

Figure 3. *Vim*$^{-/-}$ monocyte-derived alveolar macrophages are characterized by an altered transcriptional response to IAV. a) Heatmap of normalized expression of 2623 genes as defined in Figure 2. *Vim*$^{-/-}$ data was normalized to the WT mean and standard deviation (adapted z-score). **b**) Mean adapted z-scores across genes were calculated for *Vim*$^{-/-}$ expression in each cluster. **c**) Euclidean distance values were summed across all dpi for each gene and plotted as a smoothed histogram for each cluster. Dashed vertical line represents d=1.6. **d**) Bar graph representing the % genes in each cluster above the Euclidean distance cutoff (d= 1.6). **e-g**) Bar graphs representing the fold change in FPKM gene expression in *Vim*$^{-/-}$ MoAM compared to the WT mean for representative genes. (n=3-4 per group).

Supplemental Figure 3. a) Principal component analysis (PCA) of *Vim*$^{-/-}$ replicates. **b)** Violin plots representing the log2FC between *Vim*$^{-/-}$ and WT for each gene by cluster. Solid lines represent median, dotted lines represent quartiles. **c)** Volcanos plots of differentially expressed genes (edgeR p-value<0.05, and log2FC>|1.0|) between *Vim*$^{-/-}$ and WT MoAM on each day post-infection. The numbers of genes up-regulated (red) and down-regulated (blue) in *Vim*$^{-/-}$ compared to WT are given. **d)** Heatmap showing pairwise Pearson correlation of mean gene expression across replicates between each timepoint in WT and *Vim*$^{-/-}$ MoAM

Figure 4. *Vim*$^{-/-}$ MoAM downregulate M(LPS/IFNγ) genes.

a) Plot representing % of M(LPS/IFNγ) genes expressed above their WT mean at each time point (total number of genes = 103). Each dot represents a replicate. Lines represent median. **b)** Gene Set Enrichment Analysis (GSEA) enrichment plots generated using M(LPS/IFNγ) genes gene set. GSEA was performed on gene lists ranked by fold-change between WT (+) vs. *Vim*$^{-/-}$ (-) MoAM at each timepoint. Normalized enrichment scores and FDR-associated q-values are shown. **c)** Venn diagram of GSEA leading edge genes at each timepoint (84 genes total). **d)** Heatmap of adapted z-score expression of 84 genes from **C** in WT and *Vim*$^{-/-}$ MoAM. Columns represent mean of replicates. Color-coding indicates Venn diagram sections. n=3-4 per group

Supplemental Figure 4. a) Violin plots for difference of mean expression (*Vim*$^{-/-}$ - WT FPKM) of M(LPS/IFNγ) genes between *Vim*$^{-/-}$ and WT MoAM on 2-6 dpi, and between *Vim*$^{-/-}$ and WT TR-AM at baseline. Solid lines represent medians, dashed lines represent quartiles**. b)** Table of all 84 GSEA leading edge genes from **Figure 4C**. Colors match Venn diagram sections.

Figure 5. *Vim*$^{-/-}$ MoAM up-regulate Cell Cycle and M(IL-4) genes.

a) Plots representing % of cell cycle (left) and M(IL-4) (right) genes expressed above their WT mean at each time point (total number of genes = 90, 58). Each dot represents a replicate. Lines represent median. **b)** Normalized enrichment scores calculated by Gene Set Enrichment Analysis (GSEA) using cell cycle (left) and M(IL-4) (right) gene sets on gene lists ranked by fold-change between WT (+) vs. *Vim*$^{-/-}$ (-) MoAM at each timepoint. All scores were statistically significant (FDR q<0.05). n= 3-4 per group.

Supplemental Figure 5. a) Violin plots for difference of mean expression (*Vim*$^{-/-}$ - WT FPKM) of cell cycle (left) and M(IL-4) (right) genes between *Vim*$^{-/-}$ and WT MoAM on 2-6 dpi, and between *Vim*$^{-/-}$ and WT TR-AM at baseline. Solid lines represent medians, dashed lines represent quartiles**. b)** Gene Set Enrichment Analysis (GSEA) enrichment plots generated using cell cycle (top) and M(IL-4) gene sets. GSEA was performed on gene lists ranked by fold-change between WT (+) vs. *Vim*$^{-/-}$ (-) MoAM at each timepoint. Normalized enrichment scores and FDR-associated q-values are shown.

Figure 6. Vimentin-deficiency in the MoAM compartment is sufficient to protect from influenza-induced tissue damage and mortality. **a)** Schematic of experimental setup. Recipient mice (B6.SJL-Ptrprc[d]Pep3[a]/BoyJ [B6.SJL] [Pep boy] (CD45.1) were irradiated with a single dose of 1,000 cGy y-radiation, and reconstituted with bone marrow cells from either WT or *Vim*$^{-/-}$ donor mice (CD45.2) via retro-orbital injection. After a 30 day recovery period, mice were intratracheally (i.t.) infected with a lethal dose of IAV. At 5d pi, Bronchoalveolar lavage fluid (BALF) was collected and lungs were harvested for cytokine measurement, viral plaque assay, and wet/dry ratio analysis. **b)** Mice with *Vim*$^{-/-}$ bone marrow had less protein in BALF compare to those who received WT bone marrow **c)** Lungs from WT mice who received WT bone marrow have a greater wet/dry ratio at 5 dpi compared to those who received *Vim-/-* bone marrow. **d)** Viral titers were unchanged between mice who received WT vs. *Vim*$^{-/-}$ bone marrow. **e)** Mice with *Vim*$^{-/-}$ bone marrow exhibited lower levels of Il-1β, TNFα, GM-CSF, MIP-1α, IL-6, and RANTES/CCL5 compared with those who received WT bone marrow.

Supplemental Figure 6. Representative flow cytometry dot plots demonstrate successful engraftment of WT and *Vim*$^{-/-}$ CD45.2 donor cells into CD45.1 recipient mice.

Figure 1

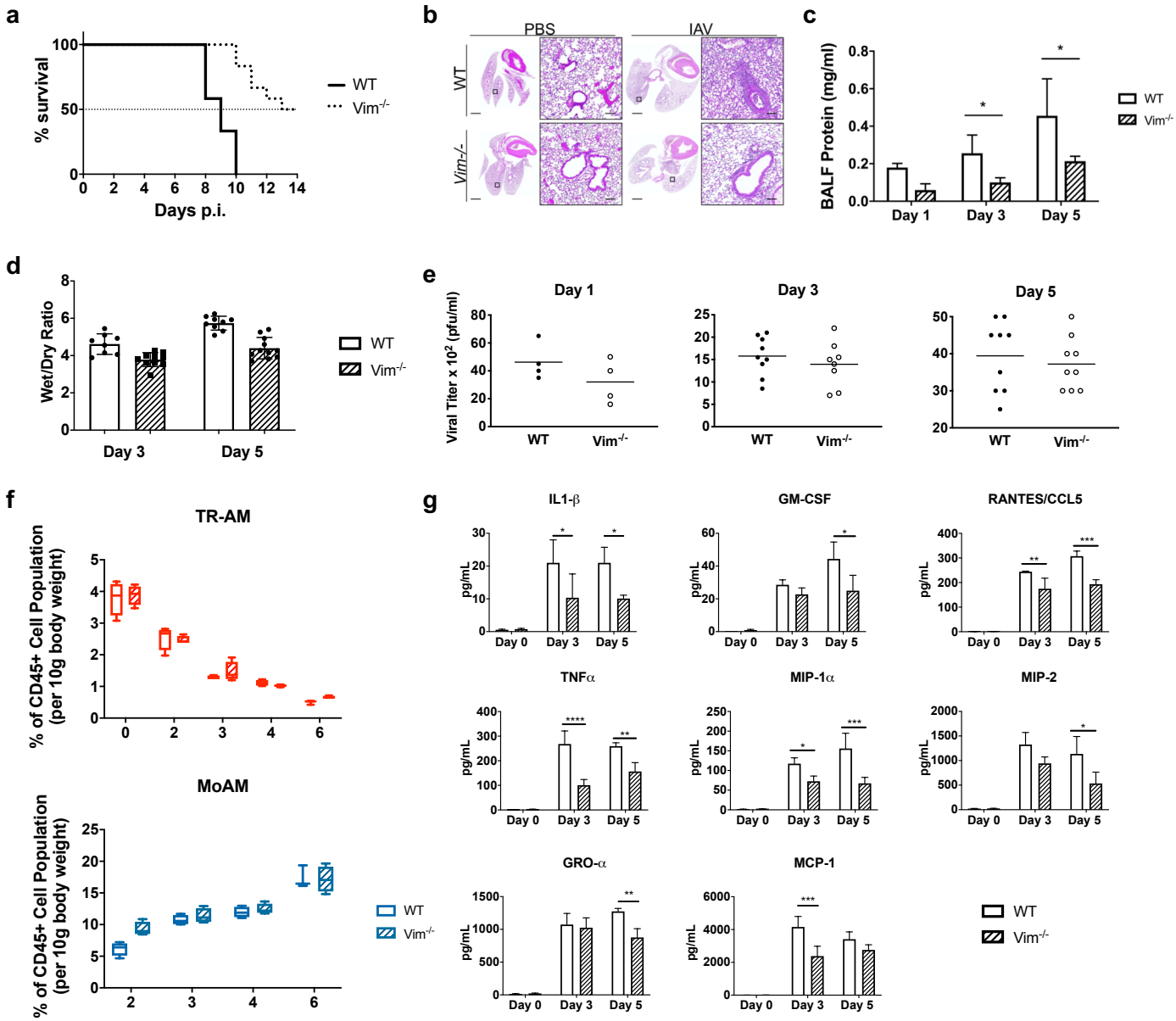
a
% survival
Days p.i.
WT
Vim-/-
b
PBS
IAV
WT
Vim-/-
c
BALF Protein (mg/ml)
Day 1
Day 3
Day 5
WT
Vim-/-
d
Wet/Dry Ratio
Day 3
Day 5
WT
Vim-/-
e
Viral Titer x 10^2 (pfu/ml)
Day 1
Day 3
Day 5
WT
Vim-/-
f
TR-AM
MoAM
% of CD45+ Cell Population (per 10g body weight)
WT
Vim-/-
g
IL1-β
GM-CSF
RANTES/CCL5
TNFα
MIP-1α
MIP-2
GRO-α
MCP-1
pg/mL
Day 0
Day 3
Day 5
WT
Vim-/-

Supplemental Figure 1

a

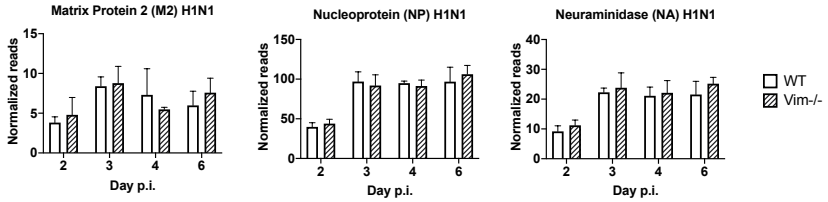

b

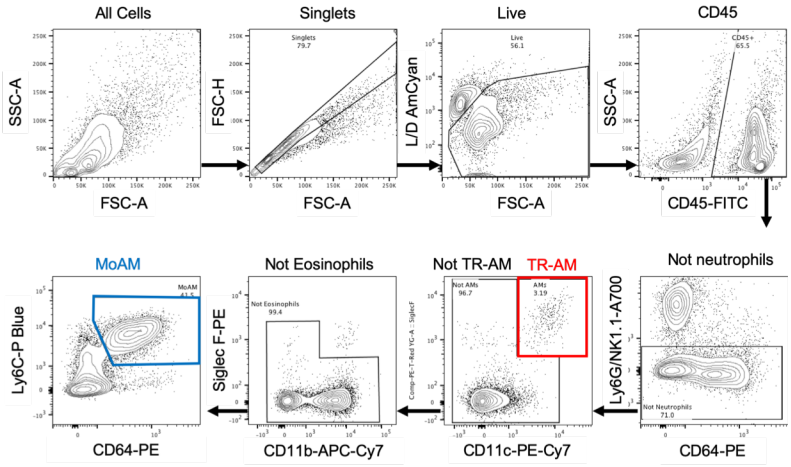

c

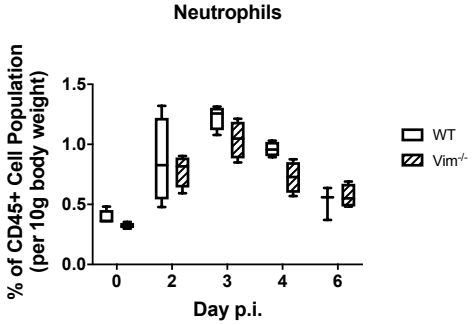

Figure 2

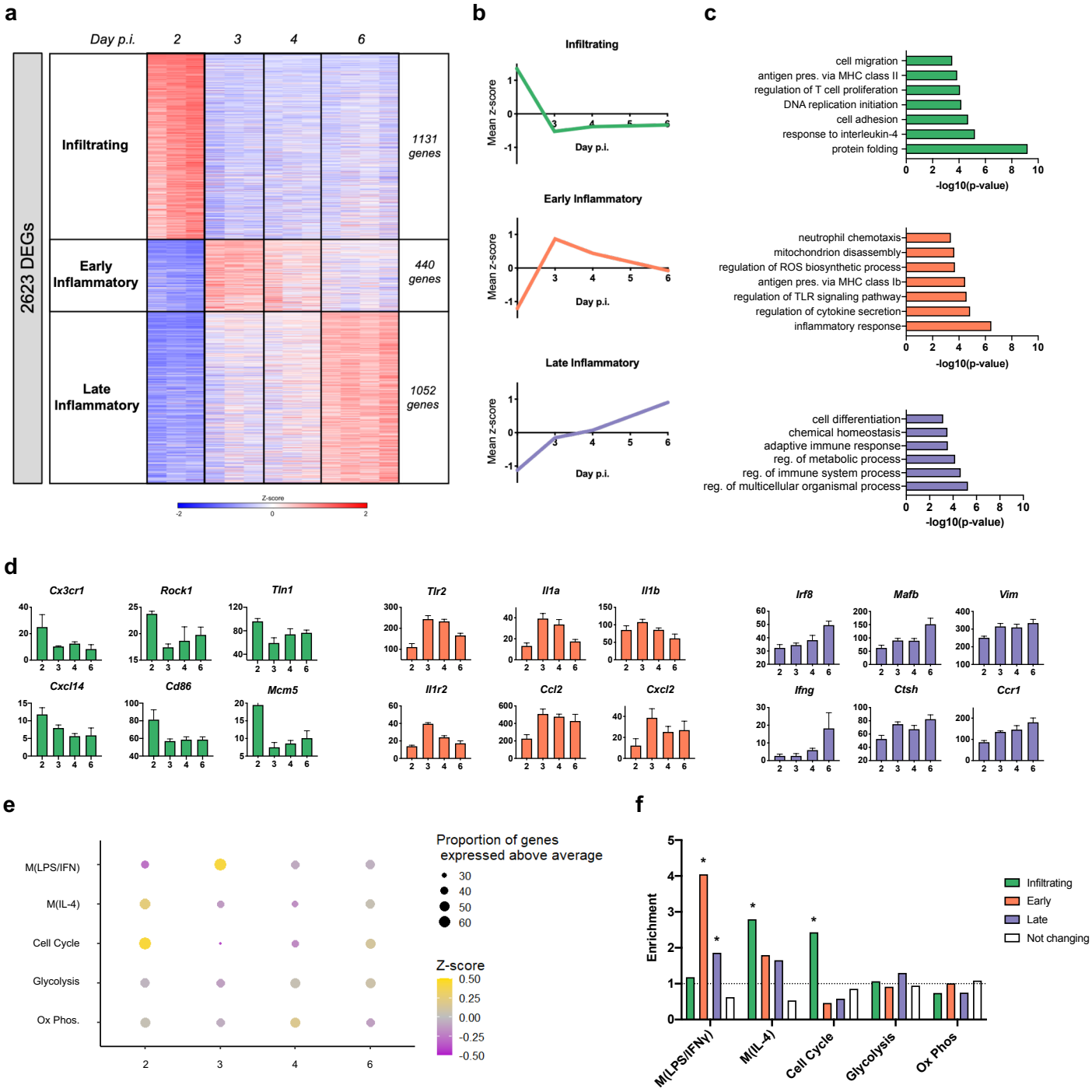
a
Day p.i.
2
3
4
6
2623 DEGs
Infiltrating
Early Inflammatory
Late Inflammatory
1131 genes
440 genes
1052 genes
Z-score
-2
0
2
b
Infiltrating
Early Inflammatory
Late Inflammatory
Mean z-score
Day p.i.
c
cell migration
antigen pres. via MHC class II
regulation of T cell proliferation
DNA replication initiation
cell adhesion
response to interleukin-4
protein folding
neutrophil chemotaxis
mitochondrion disassembly
regulation of ROS biosynthetic process
antigen pres. via MHC class Ib
regulation of TLR signaling pathway
regulation of cytokine secretion
inflammatory response
cell differentiation
chemical homeostasis
adaptive immune response
reg. of metabolic process
reg. of immune system process
reg. of multicellular organismal process
-log10(p-value)
d
Cx3cr1
Rock1
Tln1
Tlr2
Il1a
Il1b
Irf8
Mafb
Vim
Cxcl14
Cd86
Mcm5
Il1r2
Ccl2
Cxcl2
Ifng
Ctsh
Ccr1
e
M(LPS/IFN)
M(IL-4)
Cell Cycle
Glycolysis
Ox Phos.
Proportion of genes expressed above average
30
40
50
60
Z-score
0.50
0.25
0.00
-0.25
-0.50
f
Enrichment
Infiltrating
Early
Late
Not changing
M(LPS/IFNγ)
M(IL-4)
Cell Cycle
Glycolysis
Ox Phos

Supplemental Figure 2

a

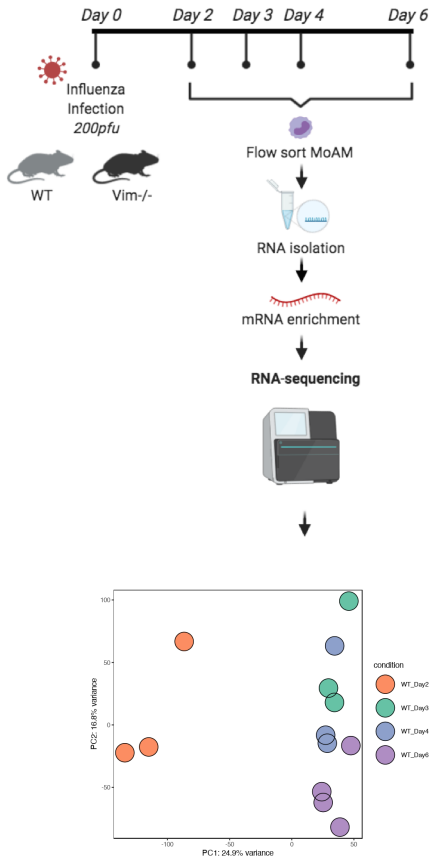

b

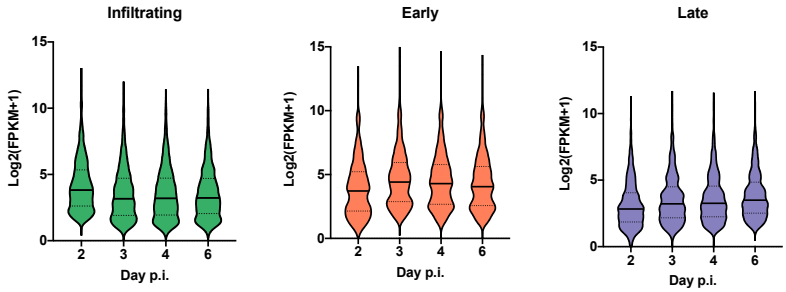

c

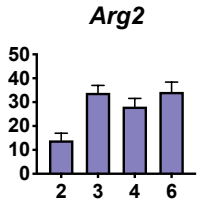

Figure 3

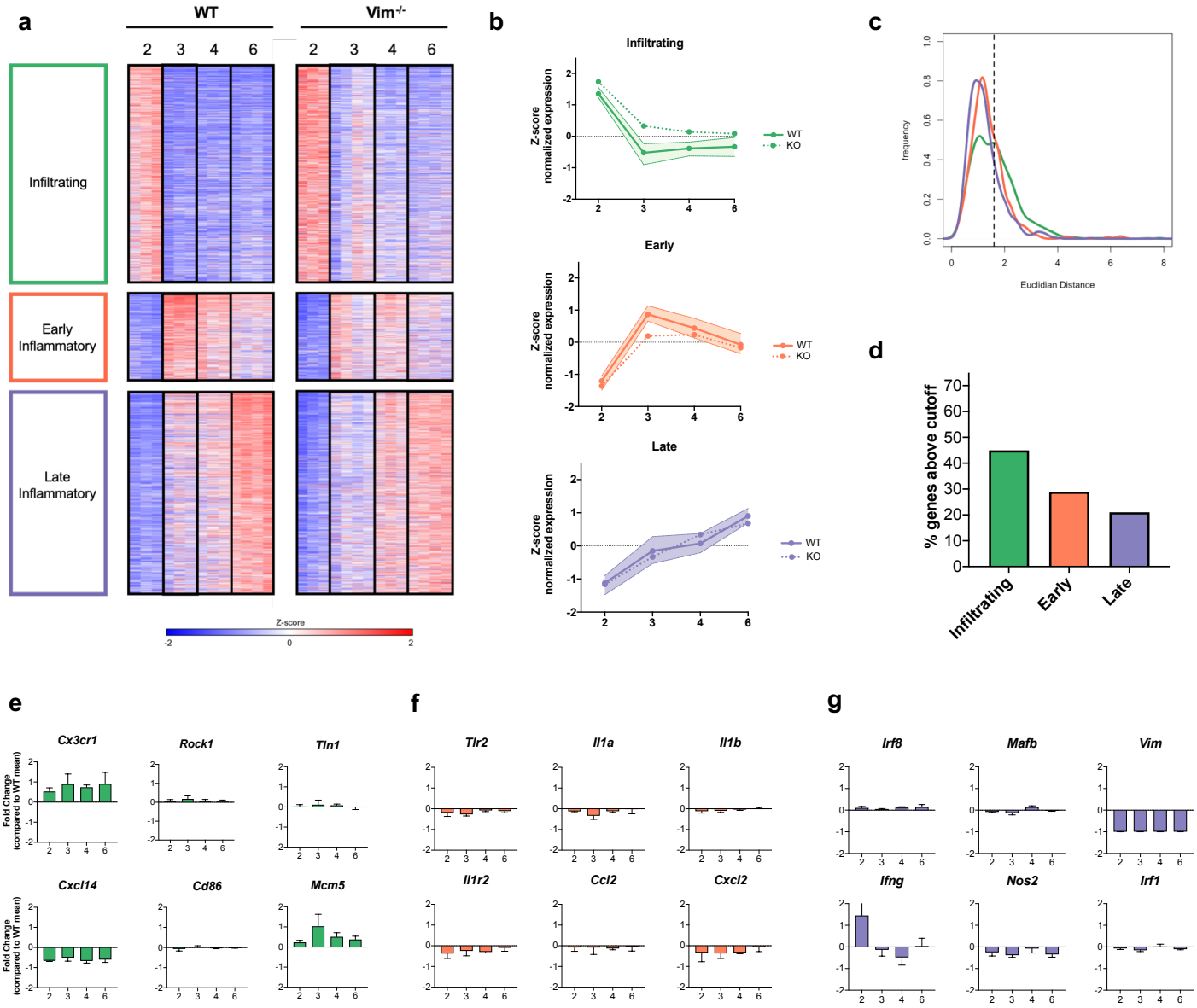
a
WT
Vim-/-
2 3 4 6
Infiltrating
Early Inflammatory
Late Inflammatory
Z-score
-2 0 2
b
Infiltrating
Early
Late
Z-score normalized expression
WT
KO
c
frequency
Euclidian Distance
d
% genes above cutoff
Infiltrating
Early
Late
e
Cx3cr1
Rock1
Tln1
Cxcl14
Cd86
Mcm5
Fold Change (compared to WT mean)
f
Tlr2
Il1a
Il1b
Il1r2
Ccl2
Cxcl2
g
Irf8
Mafb
Vim
Ifng
Nos2
Irf1

Supplemental Figure 3

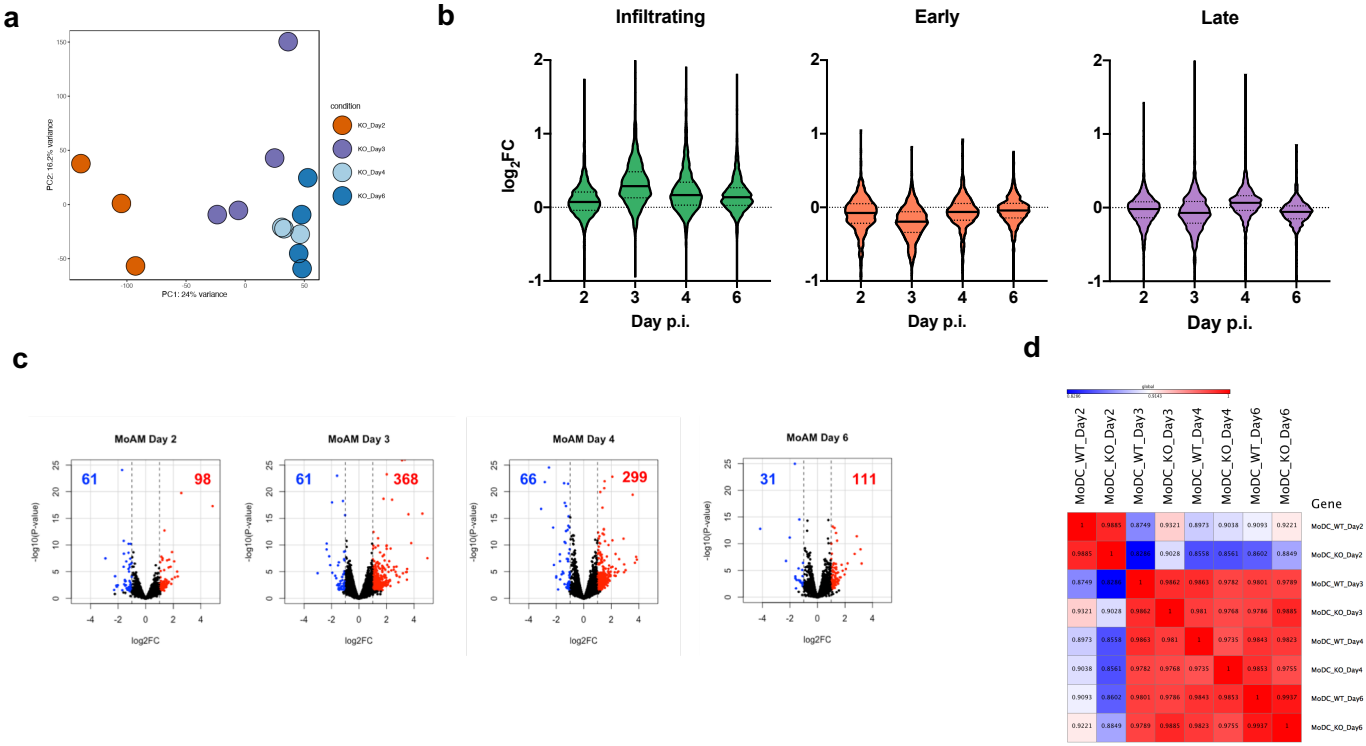

Figure 4

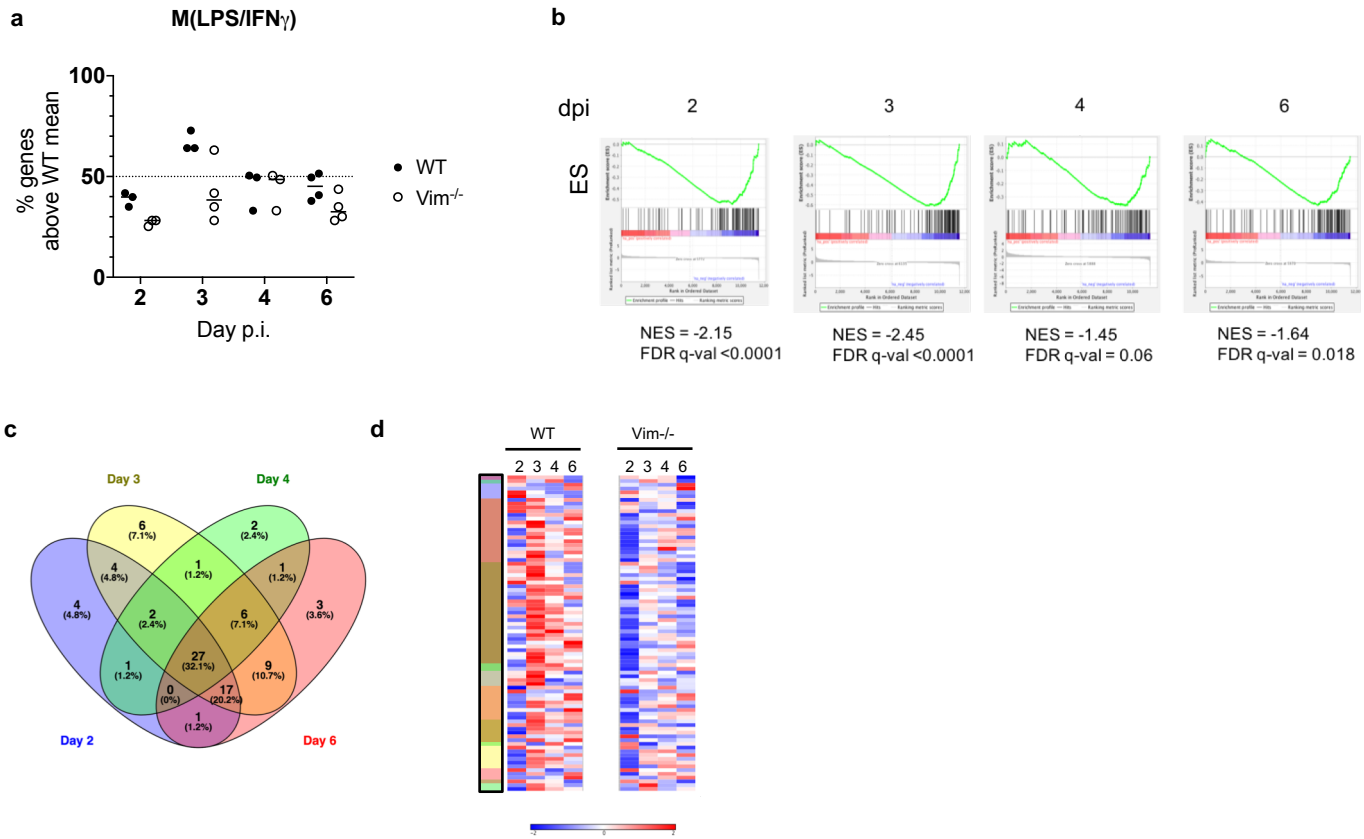
a
M(LPS/IFNγ)
% genes above WT mean
100
50
0
2
3
4
6
Day p.i.
WT
Vim-/-
b
dpi
2
3
4
6
ES
NES = -2.15
FDR q-val <0.0001
NES = -2.45
FDR q-val <0.0001
NES = -1.45
FDR q-val = 0.06
NES = -1.64
FDR q-val = 0.018
c
Day 3
Day 4
Day 2
Day 6
6 (7.1%)
2 (2.4%)
4 (4.8%)
1 (1.2%)
1 (1.2%)
4 (4.8%)
2 (2.4%)
6 (7.1%)
3 (3.6%)
27 (32.1%)
1 (1.2%)
9 (10.7%)
0 (0%)
17 (20.2%)
1 (1.2%)
d
WT
Vim-/-
2 3 4 6
2 3 4 6

Supplemental Figure 4

a

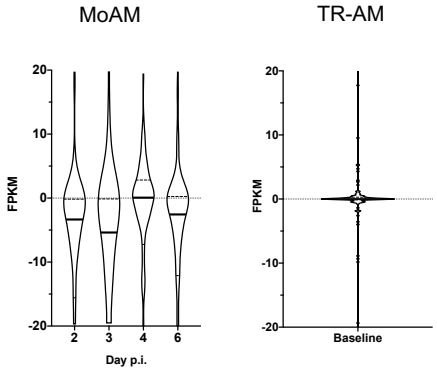

b

Ddx58	Il6	Ddx60
Cd80	Aoah	Procr
Il4ra	Ms4a4c	Il12rb1
Ptgs2	Fcgr1	Cd40
Dnase1l3	Cd38	Herc6
Stat2	Pyhin1	Mx1
Tuba4a	Oasl1	Iigp1
Ifit2	Msrb1	Tap1
Irgm2	Irg1	Clic5
Gbp5	Cxcl11	Irgm1
Slc3a2	Tlr2	Art3
Socs3	C3	Fpr2
Igtp	Cfb	Gbp11
Xaf1	Hp	Cxcl9
Arhgap24	Ccrl2	Ubd
Cd274	H2-T10	Itgal
Slfn8	Nos2	Ifi44
Slamf7	Fcgr4	Icam1
Niacr1	Cd300lf	Serpina3f
Slfn4	Pstpip2	Slfn1
Gbp4	Pydc4	Fpr1
Tgtp1	Cxcl2	Gpr18
H2-Q6	Irak3	Sct
Cxcl10	Saa3	P2rx7
Isg15	Il1b	Nrp2
Ifit1	Zbp1	Cd69
Fam26f	Ccl5	Car2
Rsad2	Marco	Upp1

Figure 5

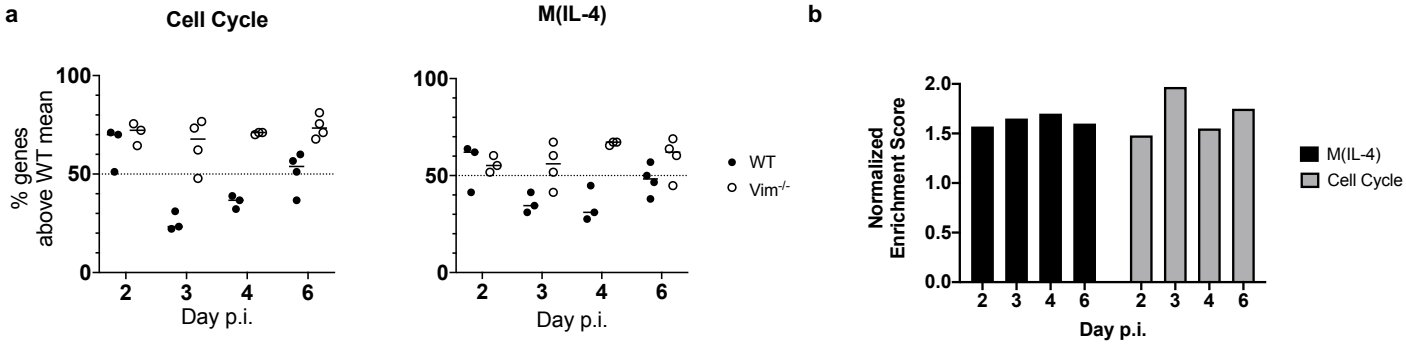
a
Cell Cycle
M(IL-4)
% genes above WT mean
100
50
0
2
3
4
6
Day p.i.
WT
Vim-/-
b
Normalized Enrichment Score
2.0
1.5
1.0
0.5
0.0
M(IL-4)
Cell Cycle

Supplemental Figure 5

a

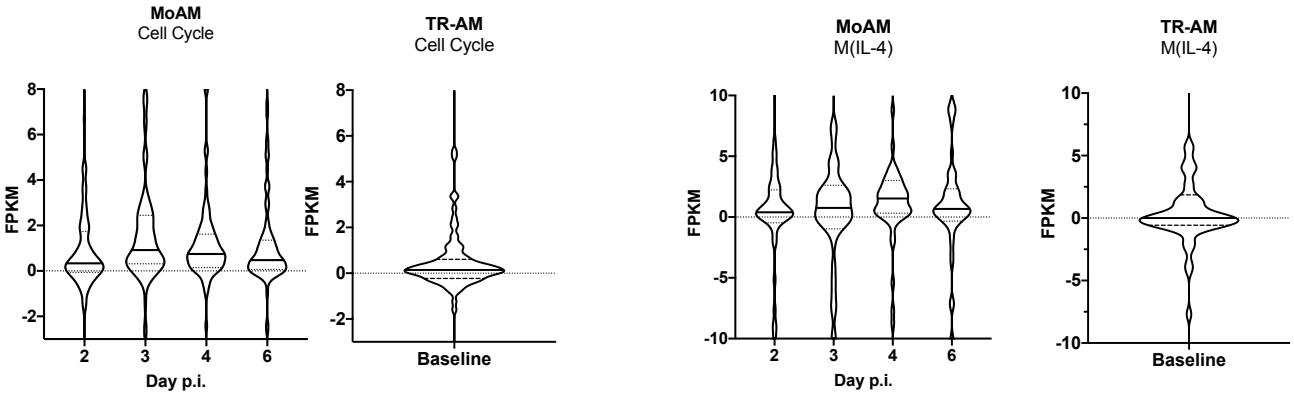

b

Cell Cycle

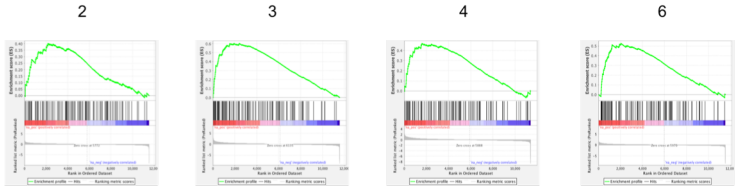

NES = 1.48
FDR q-val = 0.025

NES = 1.97
FDR q-val <0.0001

NES = 1.55
FDR q-val =0.003

NES = 1.76
FDR q-val = 0.001

M(IL-4)

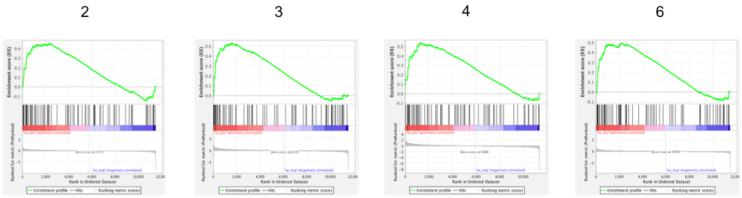

NES = 1.57
FDR q-val = 0.011

NES = 1.65
FDR q-val =0.002

NES = 1.70
FDR q-val< 0.0001

NES = 1.60
FDR q-val = 0.010

Figure 6

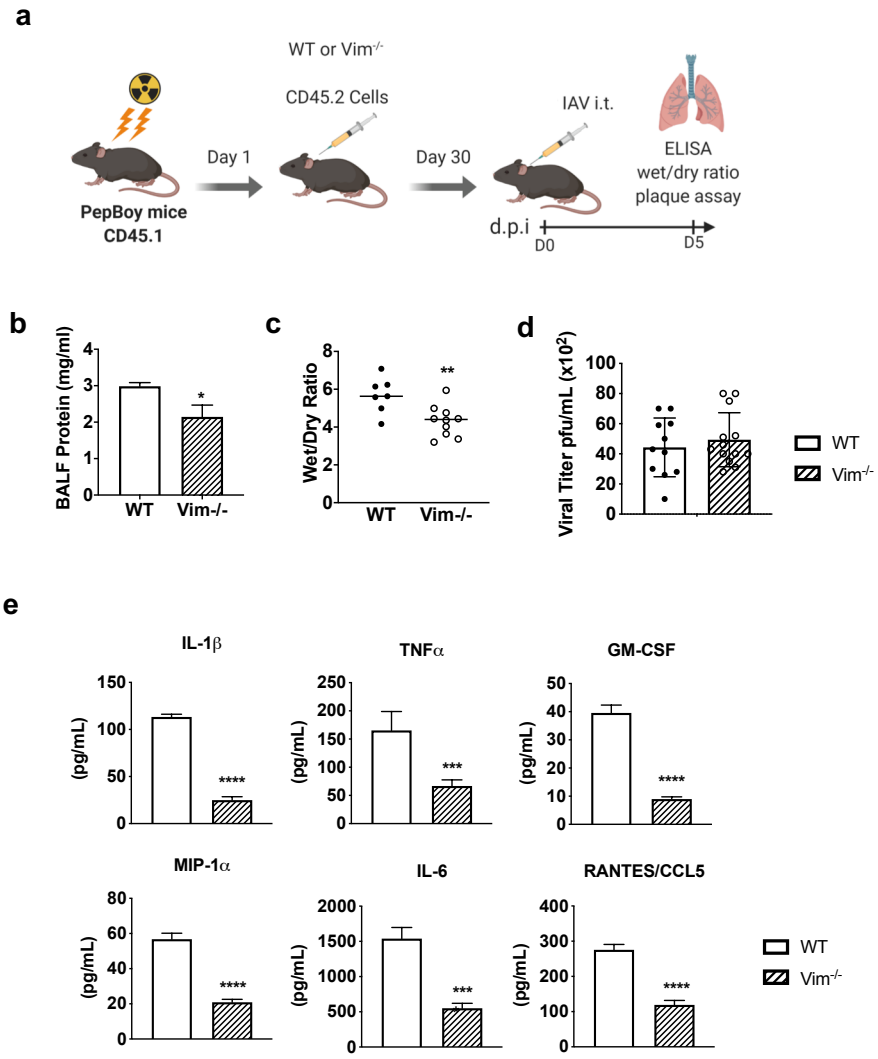
a
WT or Vim-/-
CD45.2 Cells
IAV i.t.
Day 1
Day 30
ELISA
wet/dry ratio
plaque assay
PepBoy mice
CD45.1
d.p.i
D0
D5
b
BALF Protein (mg/ml)
WT
Vim-/-
c
Wet/Dry Ratio
WT
Vim-/-
d
Viral Titer pfu/mL (x10²)
WT
Vim-/-
e
IL-1β
TNFα
GM-CSF
MIP-1α
IL-6
RANTES/CCL5
(pg/mL)
WT
Vim-/-
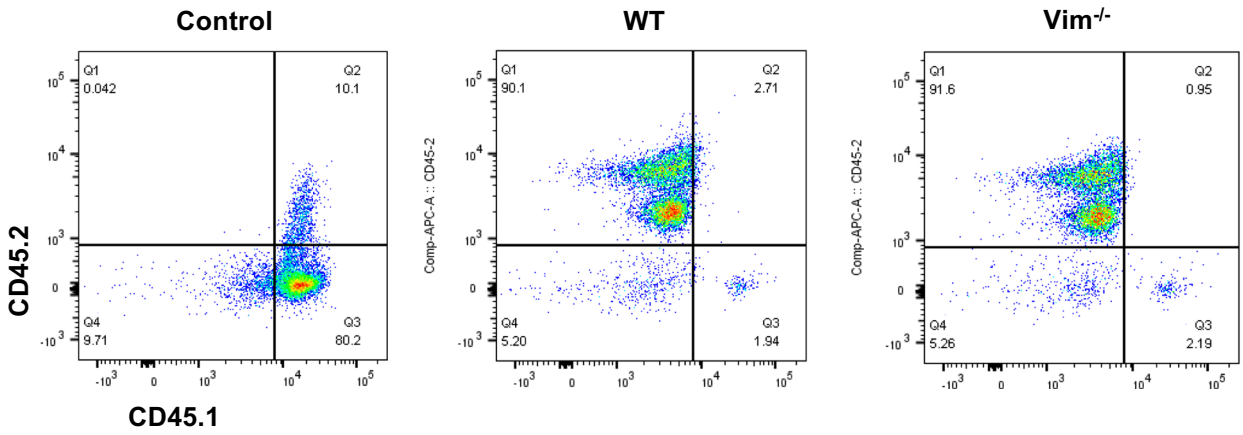
Supplemental Figure 6